

In the format provided by the authors and unedited.

Undulation enables gliding in flying snakes

Isaac J. Yeaton ^{1,4}✉, Shane D. Ross ², Grant A. Baumgardner¹ and John J. Socha ³

¹Department of Mechanical Engineering, Virginia Tech, Blacksburg, VA, USA. ²Department of Aerospace and Ocean Engineering, Virginia Tech, Blacksburg, VA, USA. ³Department of Biomedical Engineering and Mechanics, Virginia Tech, Blacksburg, VA, USA. ⁴Present address: Johns Hopkins University Applied Physics Laboratory, Laurel, MD, USA. ✉e-mail: Isaac.Yeaton@jhuapl.edu

Supplementary Information

Undulation enables gliding in flying snakes

Isaac J. Yeaton^{1,*}, Shane D. Ross², Grant A. Baumgardner¹ and John J. Socha³

¹Department of Mechanical Engineering

²Department of Aerospace and Ocean Engineering

³Department of Biomedical Engineering and Mechanics

Virginia Tech

*Current affiliation: Johns Hopkins University Applied Physics Laboratory
Isaac.Yeaton@jhuapl.edu

Video legends

Supplementary Video 1

Side view of a long glide of the flying snake *Chrysopelea paradisi*. This slow-motion sequence shows the snake progress through the ballistic dive to the shallowing glide to landing. The sequence begins with the snake approximately 15 m above the ground, in the extended position just after a J-loop take-off (which was not recorded). During the ballistic dive, the tail is relatively up and the head is down in the pitch axis. As the snake undulates and the glide angle (relative to horizontal) decreases, the tail and posterior body move downward but continuously translate periodically in the vertical axis. Recorded in Penang, Malaysia, 2010, by producer Robert Wise, cameraman John Benam, and Jake Socha. Video provided courtesy of National Geographic Television.

Supplementary Video 2

Side view of take-off and flattening of the flying snake *Chrysopelea paradisi*. This slow-motion sequence shows the snake begin a glide using a J-loop take-off, become dorsoventrally flattened, and then gather the body into an S-shape as it falls through the ballistic dive portion and begins undulating. The body flattening that produces the snake's aerial cross-sectional shape starts during the jump and is completed just after the snake becomes fully airborne. Recorded

in Sabah, Malaysia, 2015, by producer Simon Bell, cameraman Pete McCowen, and Jake Socha. Video provided courtesy of the British Broadcasting Corporation.

Supplementary Video 3

Front view of take-off and flattening of the flying snake *Chrysopelea paradisi*. This slow-motion sequence shows the snake begin a glide using a J-loop take-off, become dorsoventrally flattened, and then gather the body into an S-shape as it falls through the ballistic dive portion and begins undulating. The snake appears momentarily ribbon-flat as it completes the jump, but this appearance results from the overexposure of the dorsal surface of the snake next to the bright sky. Near the end of the sequence, small bumps can be seen on the body near the tail; these bumps are sub-surface parasites that occur naturally in some wild-caught specimens. Recorded in Sabah, Malaysia, 2015, by producer Simon Bell, cameraman Pete McCowen, and Jake Socha. Video provided courtesy of the British Broadcasting Corporation.

Supplementary Video 4

Overhead view of a glide trial of the flying snake *Chrysopelea paradisi*. Recorded with two Photron APS-RX high-speed video cameras. This glide is from a snake with a mass of 71 g and snout-vent length of 77 cm.

Supplementary Video 5

Infrared markers tracked through a glide of the flying snake *Chrysopelea paradisi*. Top and side views are shown of 12 points on the snake as it moves through its trajectory.

Supplementary Video 6

Development of a 3D model of the flying snake *Chrysopelea paradisi* from motion-capture data. The interactive online visualization of the snake can be found in Visualization 1: <https://sketchfab.com/models/5aea787df31d48e288915b94e3a4c9de>.

Supplementary Video 7

Simulations of a flying snake gliding with and without aerial undulation. The co-moving frame, located at the center of mass, is indicated by the three orthogonal arrows (red, green, and blue), and the inertial coordinate system is indicated by the long lines. The instantaneous center of mass velocity is shown by the black arrow. The sheets emanating from the body are the local lift (blue) and drag (yellow) forces distributed over the body. In the first simulation, the undulating

snake (*Chrysopelea paradisi*, $f = 1.2$ Hz) pitches down, but it glides 10 m vertically before any Euler angle exceeds 85° , indicating that the snake is relatively stable over short distances. In the second simulation, the snake has the same initial conditions as in the first, but with an undulation frequency of 0 Hz. The horizontal and vertical waves were selected such that the glide is generally stable in pitch. However, the snake is still unstable, as it yaws to the left more than 85° before falling 10 m vertically.

Interactive online visualizations of aerial undulation in flying snakes

Visualization 1

<https://sketchfab.com/models/5aea787df31d48e288915b94e3a4c9de>

Reconstructed wing-body of *C. paradisi* #81 (trial 507), from the indoor glide experiments. The snake's mass is 107.2 g and snout-vent length is 85 cm. Snake 81 was the heaviest individual tested. The visualization shows the time-varying body posture as the animal glides through the arena. From the analysis presented in the main text, this trial has the following average spatial and temporal wave characteristics: undulation frequency: 1.15 Hz, number of spatial periods of bending: 1.46, horizontal wave amplitude: 98° , vertical wave amplitude: 31° , dorsoventral bending angle: 12° .

Visualization 2

<https://sketchfab.com/models/b52b079936c24494aa9d14090c1e0236>

Reconstructed wing-body of *C. paradisi* #95, (trial 618), from the indoor glide experiments. The snake's mass is 37.3 g and snout-vent length is 64.4 cm. Snake 95 was the lightest individual tested. The visualization shows the time-varying body posture as the animal glides through the arena. From the analysis presented in the main text, this trial has the following average spatial and temporal wave characteristics: undulation frequency: 1.33 Hz, number of spatial periods of bending: 1.07, horizontal wave amplitude: 112° , vertical wave amplitude: 28° , dorsoventral bending angle: -20° .

Supporting material for main manuscript results

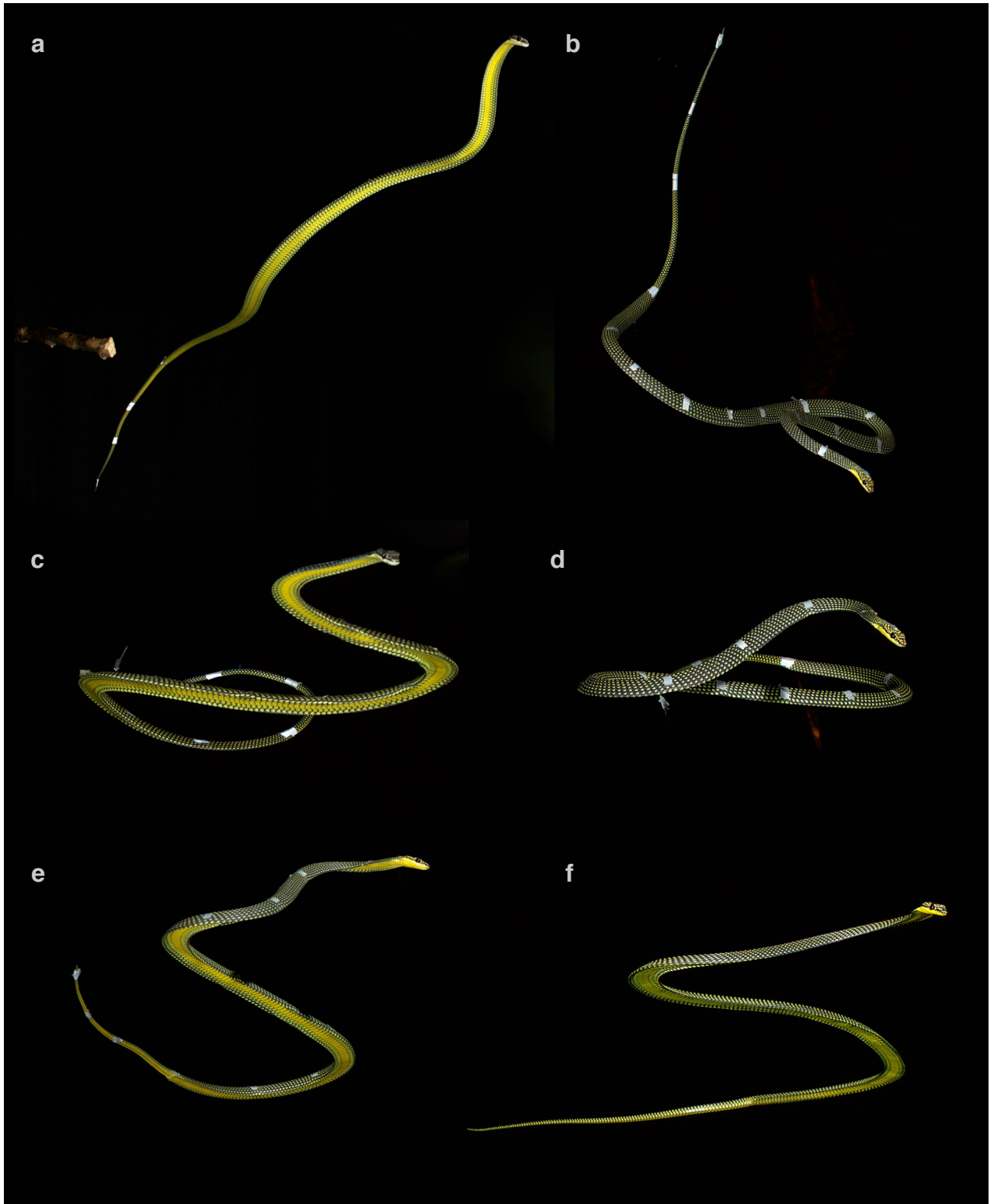


Figure S1: Representative images of flying snakes in the air during experiments. Caption on next page.

Figure S1: Representative images of flying snakes in the air during experiments in The Cube at Virginia Tech. All images are of *Chrysopelea paradisi*. Snakes in a-e are marked with infrared-reflective tape on the dorsal skin; the snake in (f) was unmarked for comparison. The snake in (a) is fully extended just after take-off from the branch on the left. The snake in B has begun undulating, but is in the early ballistic phase of the trajectory with the tail up and the anterior body pitched downward. The snakes in c-f are fully undulating. Images were captured using a DSLR camera (D800E, Nikon) with a 50 mm lens (AF-S NIKKOR 50mm f/1.8G, Nikon) and two high-speed flashes (Einstein E640, Paul C. Buff, Inc.).

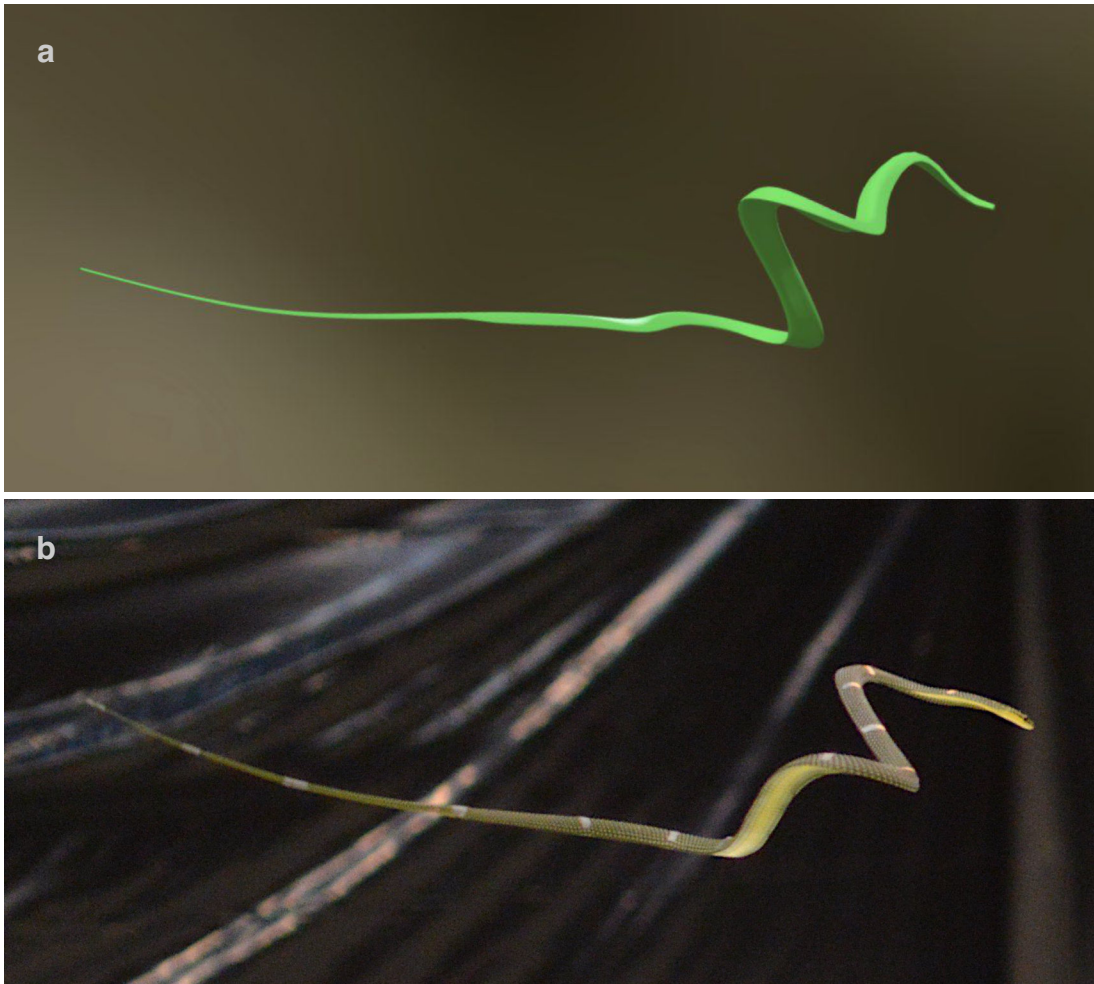


Figure S2: **Qualitative comparison of the model snake vs. a real flying snake during a glide trial.** The image of the model snake (a) is a frame grab from Visualization 1 (at time point 10:95), accessible online at <https://sketchfab.com/3d-models/507-81-sc-obj-no-pts-10x-5aea787df31d48e288915b94e3a4c9de>. The photo of the real snake (b) shows the specimen 2 m above the ground, after a vertical travel of 6 m. The two images are from different trials.

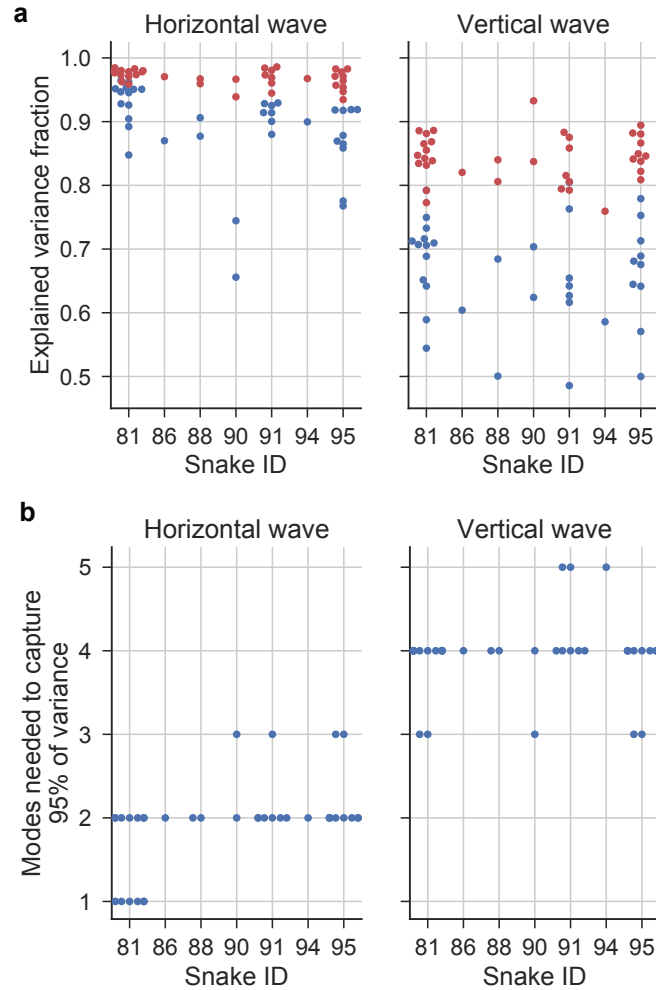


Figure S3: **Summary of complex orthogonal decomposition analysis.** (a) The explained variance fraction for each snake for the horizontal and vertical waves. Summing all modes results in a variance fraction of 1 (explaining all of the modal activity). The blue dots are the explained variance fraction for the first mode alone, and the red dots are the explained variance of the first and second modes combined. The horizontal wave is more organized, with a single mode accounting for much of the variance. (b) The number of modes required to account for 95% of the variance. Generally, two modes are required for the horizontal, and three or four modes are required for the vertical wave.

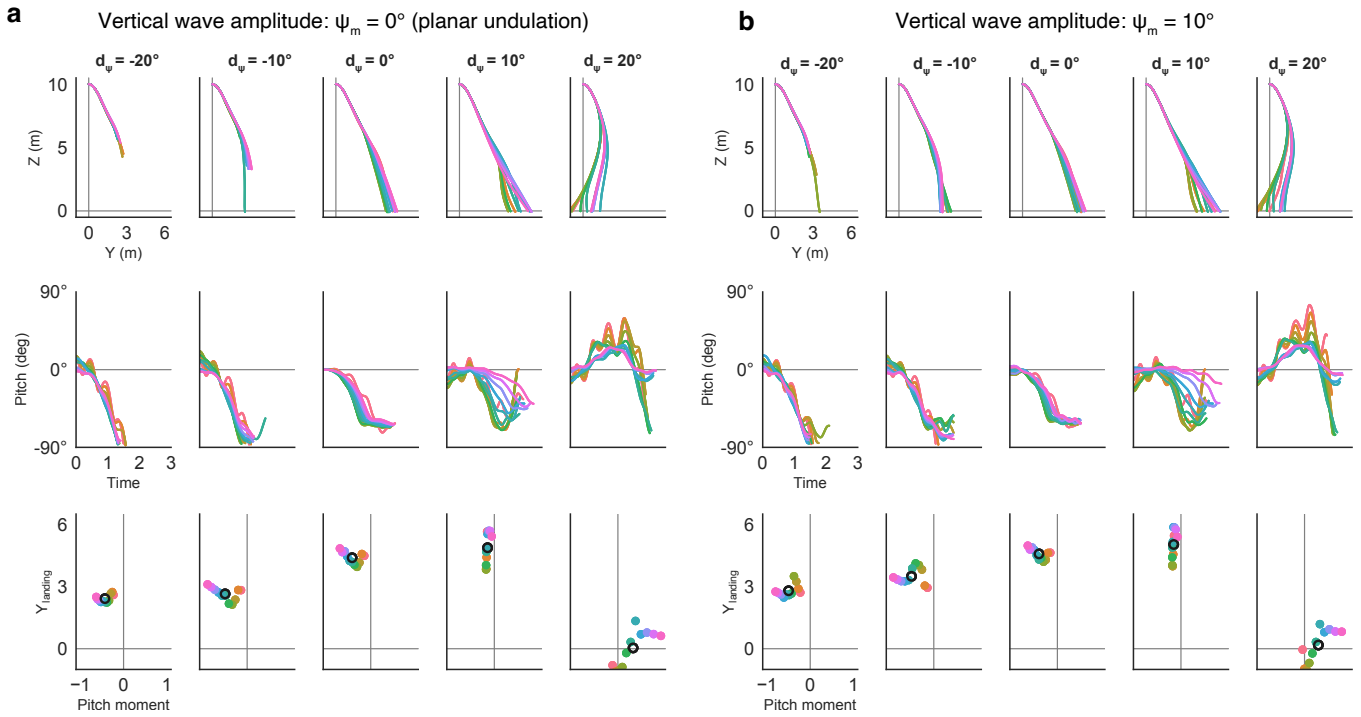


Figure S4: **Effect of the vertical wave amplitude ψ_m and dorsoventral bending d_ψ (columns) on glide performance for different dorsoventral flexion angles and number of spatial periods.** See Manuscript Fig. 5 for details. **(a)** Simulated glides with planar undulation performed worst, although the behavior for different dorsoventral bending angles (moving across the columns) is the same in **(b)** for $\psi_m=10^\circ$. Negative dorsoventral bending is associated unstable glides and poor performance due to pitching down and a net negative phase-averaged pitch moment. Positive dorsoventral bending is associated with stable glides with poor performance due to pitching-up. The pitch moment is in units of Nmm.

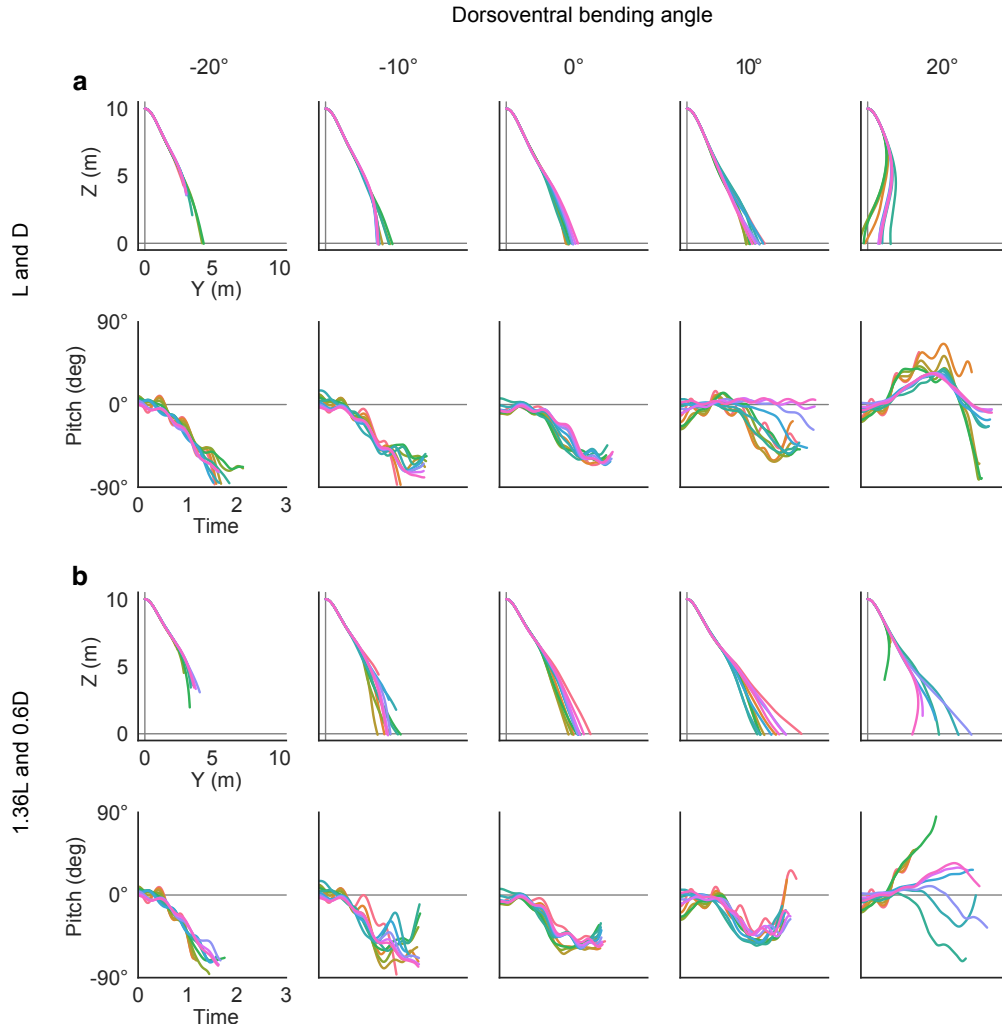


Figure S5: **Effect of modified lift and drag coefficients on simulated glide stability as dorsoventral bending is varied.** See Manuscript Fig. 5 for details. **(a)** Stability results, showing the side view of the center of mass position and time history of pitching angle, as the dorsoventral bending angle is varied. Different colors indicate different ν_θ and θ_m combinations. Reproduced from Fig. 5. **(b)** Analogous stability results, but with the lift coefficient increased by 36% and the drag coefficient decreased by 40% compared to the aerodynamic model in Fig. S7. Glides with higher lift and lower drag travel farther, but the stability trends are the same as the glides with unmodified force coefficients. Glides with negative dorsoventral bending angle become unstable in pitch and do not reach the ground. As dorsoventral bending angle increases, there is less pitching downward and glides cover more horizontal distance. If dorsoventral bending increases too much, the trajectory is forced backwards.

Table S1: Overview of flying snake simulations shown in Fig. 4 , demarcated by the different shape space regions of ‘open’, ‘observed’, and ‘closed’ shapes (Fig. 4b).The fraction of stable glides and increase in horizontal and vertical distance travelled all depend on location within the shape space.

Metric	Figure	All Shapes	Observed Shapes	Open Shapes	Closed Shapes
Percent stable (0 Hz)	4c	49.6%	34.7%	83.3%	36%
Percent stable (1.2 Hz)	4d	94.2%	100%	100%	80.6%
Glide distance (0 Hz)	4f	4 m	4 m	4.2 m	3.7 m
Glide distance (1.2 Hz)	4g	4.3 m	4.9 m	3.4 m	4.2 m
Vertical distance increase (75 m)	4e	10.5 m	12.5 m	13.8 m	4.5 m
Horizontal distance increase (75 m)	4h	5 m	6.9 m	5.9 m	1.8 m

Support figures for main manuscript methods

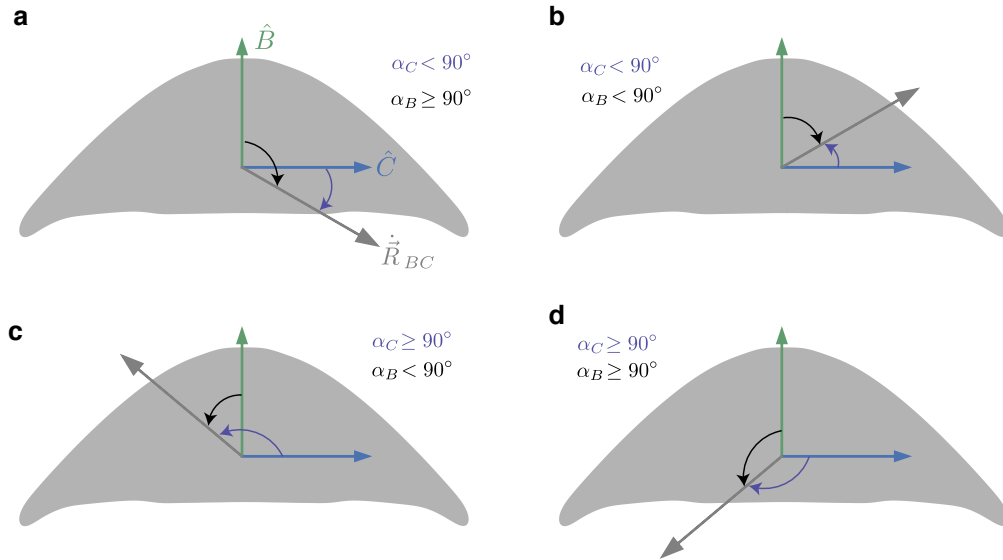


Figure S6: Angle of attack and lift vector direction based on the orientation of the body with the free-stream airflow. (a)–(d) match the cases described in the Methods section “Aerodynamic lift and drag”.

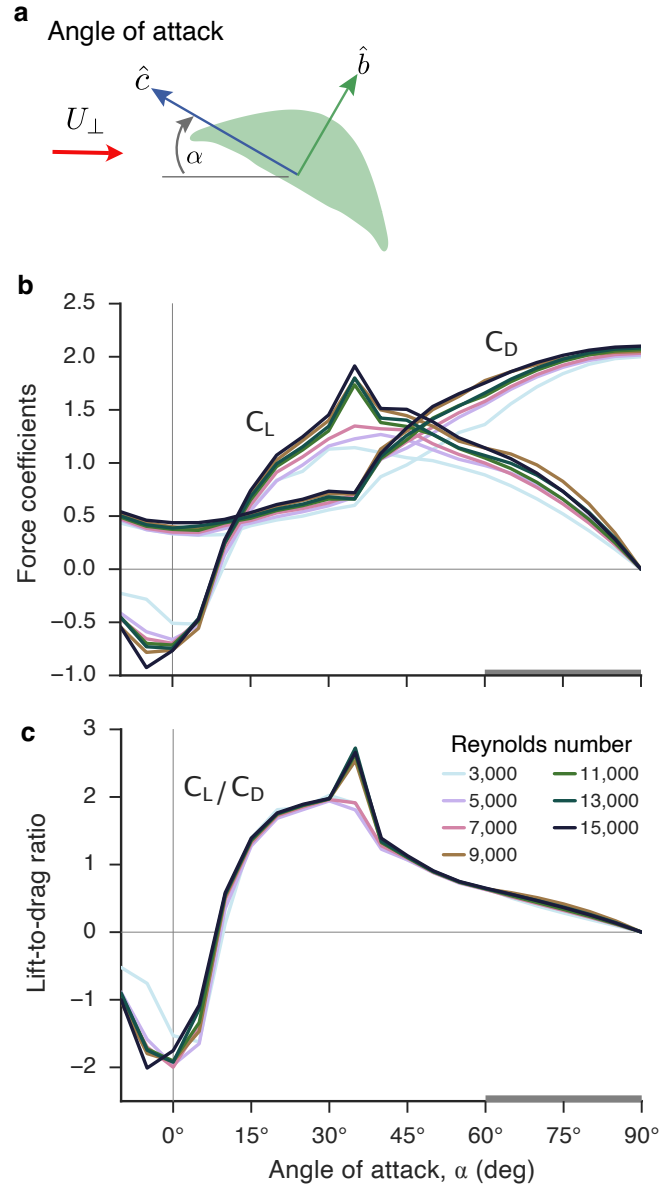


Figure S7: **Lift and drag coefficients of flying snakes used in this study.** (a) Definition of the angle of attack, α , as the angle between the chord-line direction \hat{c} and the velocity component locally perpendicular to the body. The data below 60° are from [1]. The extrapolated region is demarcated by the gray band on the horizontal axis between 60° and 90° . (b) Lift and drag coefficients as functions of angle of attack and Reynolds number. The extrapolated region (between 60° and 90°) is demarcated by the gray band on the horizontal axis. (c) Lift-to-drag ratio, with the characteristic peak at an angle of attack of 35° .

Additional methods details

Snake morphometrics

We used measured width and mass distributions of *C. paradisi* to make the model more anatomically accurate (Fig. S8). We measured the width distribution of flying snakes from mid-glide silhouette images acquired from a previous experiment [2, 3]. From underside views of each snake, the images were thresholded to separate the snake from the background. The Euclidean distance transform (EDT) was used to quantify the distance of each pixel within the thresholded snake body to the edge; the midline of the snake has the largest EDT value. The midline was found by skeletonizing the thresholded image such that the image was a continuous line one pixel wide; the EDT was then sampled along the skeleton. Pixel distances were scaled to physical units using the arc-length of the snake, found by integrating distance along the skeleton. Width distributions were measured from six images from three different animals and averaged together for one width distribution. A bias correction was applied to the width distribution, as the maximum width from the above procedure was 3% lower than the maximum width reported for the snakes imaged. The bias in width is likely caused from the thresholding process removing pixels near the edge of the snake.

We measured the linear mass density of flying snakes by sectioning three frozen snakes that had passed away from natural causes. The snakes were cut into approximately 10 mm sections and each piece was weighed with a scale (AL104 Analytical Balance, Mettler Toledo) with an accuracy of ± 0.1 mg. The mass distribution for each animal was normalized by the average density, $\bar{\rho} = m_{\text{total}}/\text{SVL}$, and then averaged. The width and mass density distributions were fit with second-order polynomials for use in the simulation. The mass density was fit with two parabolas because the head was comparatively more massive (per length) than the body.

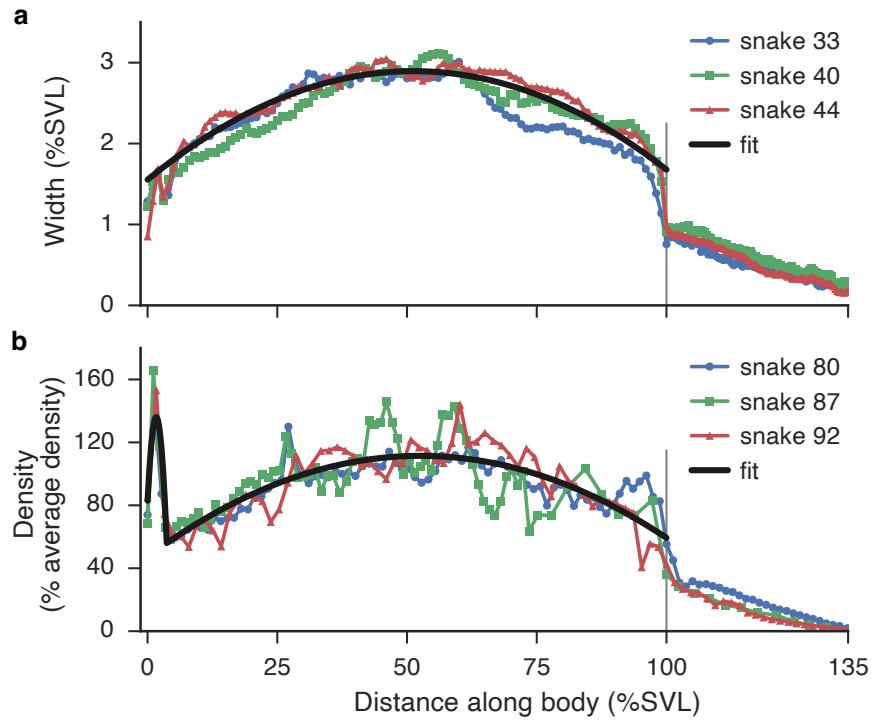


Figure S8: Width and mass distributions of flying snakes. **(A)** Width distribution along the length of the animal as percent of the snout-vent length (SVL) of the snake for three different animals, and a parabolic fit. **(B)** Density distribution as percent of the average linear snake density, $\bar{\rho} = m_{tot}/SVL$ for three different snakes. The head has higher density than the body, but both are modeled by two parabolas. The tail is shown, but the tail dynamics were not modeled.

Complex orthogonal decomposition

Here we provide details of complex orthogonal decomposition and how it was used to quantify the horizontal and vertical waves. For a full discussion, see [4–6]. We begin with the horizontal and vertical bending angle data in 2D form,

$$\Theta = \begin{bmatrix} \bar{\theta}_1 & \bar{\theta}_2 & \dots & \bar{\theta}_n \\ | & | & & | \\ | & | & & | \\ | & | & & | \\ | & | & & | \end{bmatrix} \quad (\text{S1})$$

$$\Psi = \begin{bmatrix} \bar{\psi}_1 & \bar{\psi}_2 & \dots & \bar{\psi}_n \\ | & | & & | \\ | & | & & | \\ | & | & & | \\ | & | & & | \end{bmatrix} \quad (\text{S2})$$

where each column of Θ and Ψ are the horizontal and vertical waves sampled at times t_1, \dots, t_n , and each row is the spline location from s_1, \dots, s_m . At each time point, the horizontal wave has the mean removed, and the vertical wave has the mean and a linear fit removed. Each matrix is of size $m \times n$.

The decomposition method requires converting the measured signals Θ and Ψ into complex analytic signals using the Hilbert transform. This transform is performed along the rows of the measured bending angles, i.e., how the angle at a particular location along the body varies in time. Denoting the Hilbert transform as \mathcal{H} and the complex analytic signal as \mathbf{z} , we have

$$\mathbf{z}_\theta(s_i, t) = \mathcal{H}(\bar{\theta}(s_i, t)) \quad (\text{S3})$$

$$\mathbf{z}_\psi(s_i, t) = \mathcal{H}(\bar{\psi}(s_i, t)) \quad (\text{S4})$$

where $1 \leq i \leq m$, where m is the number of points the spline is evaluated at. We then form the complex ensemble matrix \mathbf{Z} as

$$\mathbf{Z} = \begin{bmatrix} | & | & \dots & | \\ \mathbf{z}_1 & \mathbf{z}_2 & \dots & \mathbf{z}_n \\ | & | & & | \end{bmatrix} \quad (\text{S5})$$

The i th row of \mathbf{Z} is the time series of the bending angle at the i th location along the body. The complex ensemble matrix is of size $m \times n$. We then form the complex correlation matrix,

$$\mathbf{R} = \frac{\mathbf{Z}\bar{\mathbf{Z}}^T}{n} \quad (\text{S6})$$

where the overbar indicates complex conjugation and \mathbf{R} is of size $m \times m$. Complex orthogonal

decomposition requires solving the eigenvalue problem

$$\mathbf{R}\mathbf{W} = \lambda\mathbf{W} \quad (\text{S7})$$

where the columns of \mathbf{W} (size $m \times m$) are the eigenvectors called the complex orthogonal modes and the m eigenvalues λ are called the complex orthogonal values. We sort the eigenvalues based on their magnitude and then rearrange the columns of \mathbf{W} accordingly. The motion associated with each complex orthogonal mode is found using the complex modal coordinate ensemble \mathbf{Q} . The complete analytical signal can be recovered as

$$\mathbf{Z} = \mathbf{Q}\mathbf{W} \quad (\text{S8})$$

where the columns of \mathbf{W} are the modal vectors and the rows of \mathbf{Q} (size $m \times n$, same as \mathbf{Z}) are samples of the modal coordinates. Solving for \mathbf{Q} ,

$$\mathbf{Q} = \mathbf{W}^{-1}\mathbf{Z} = \bar{\mathbf{W}}^T\mathbf{Z} \quad (\text{S9})$$

Quantifying aerial undulation

The complex orthogonal modes (columns of \mathbf{W}) encompass the spatial characteristics of the bending waves, and the complex modal coordinate ensemble (rows of \mathbf{Q}) encompass the temporal wave characteristics. Both matrices are complex. The units of \mathbf{Q} are time; \mathbf{W} is unitless and must be scaled by $\sqrt{\lambda}$ to have units of degrees. We use the mean whirl rate — how each mode moves in the complex plane (Fig. S9A,B) — to quantify the horizontal and vertical waves. For the analysis presented in the paper, we use the first (dominate) mode for each wave. To quantify the whirl rate, we ‘unwrap’ each mode by calculating the angle of each mode in the complex plane,

$$\angle W = \tan^{-1} \frac{\text{Im}(W)}{\text{Re}(W)} \quad (\text{S10})$$

$$\angle Q = \tan^{-1} \frac{\text{Im}(Q)}{\text{Re}(Q)} \quad (\text{S11})$$

which we unwrap such that there are no 2π discontinuities. The slope of $\angle W$ with respect to s is the number of spatial periods ν , and the slope of $\angle Q$ with respect to t is the undulation frequency f (Fig. S9C,D). The number of spatial periods, ν , is found by the slope of a linear fit

to the unwrapped mode \mathbf{w} against the non-dimensional arc-length s/SVL as

$$\nu_\theta = \frac{m_{\mathbf{w},\theta}}{2\pi} \quad (\text{S12})$$

$$\nu_\psi = \frac{m_{\mathbf{w},\psi}}{2\pi} \quad (\text{S13})$$

The undulation frequency is found from the slope of the best-fit line to the unwrapped \mathbf{q} against time as

$$f_\theta = \frac{m_{\mathbf{q},\theta}}{2\pi} \quad (\text{S14})$$

$$f_\psi = \frac{m_{\mathbf{q},\psi}}{2\pi} \quad (\text{S15})$$

where m is the slope. The spatial and temporal frequency ratios are therefore ν_ψ/ν_θ and f_ψ/f_θ , respectively (Fig. 2e).

The horizontal and vertical wave amplitudes (Fig. 2f,g) are found by reanimating the horizontal and vertical waves using enough modes to recover 95% of the observed variance (Fig. S3). This procedure removes noise present in the higher modes and the full waveforms. Each mode is reanimated separately and then combined together to form the filtered signal. For each mode k

$$\mathbf{z}_k(t) = \sqrt{\lambda_k} e^{2\pi f_k t i} \mathbf{w}_k \quad (\text{S16})$$

for $t_1 \leq t \leq t_n$. Each frequency component is found as described above, and the modal shapes \mathbf{w} are from columns of \mathbf{W} . Between two and four modes are combined to form the complex filtered signal, and the resulting real signal is recovered as $Re(\mathbf{z}_k(t))$. The amplitude is found as half of the average peak-to-peak value.

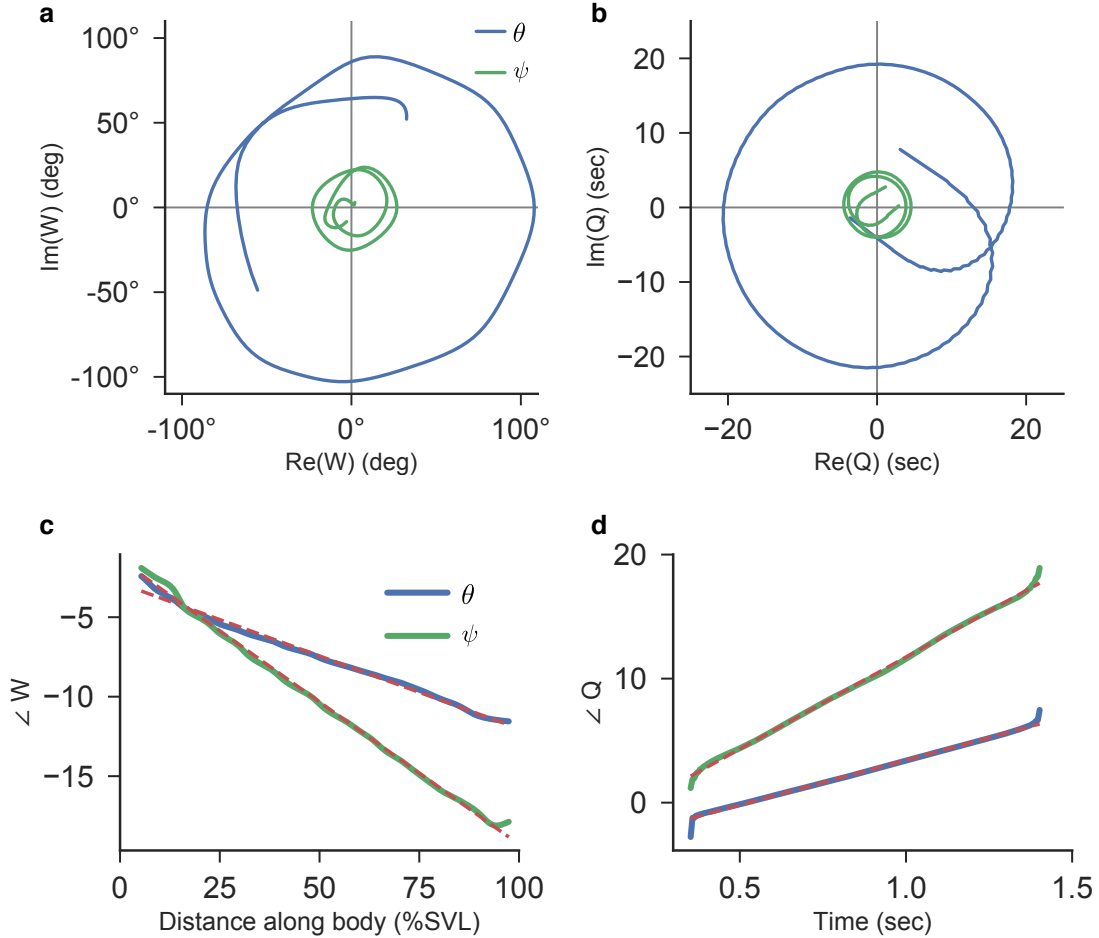


Figure S9: **Overview of complex orthogonal decomposition analysis for the glide shown in Manuscript Fig. 2.** (a) First scaled complex orthogonal model, $\sqrt{\lambda_1} \mathbf{w}_1$ for the horizontal (θ) and vertical (ψ) waves. The diameter of the circular spectrum is roughly the peak-to-peak amplitude of the waves (Fig. 2a). One revolution indicates one complete period of bending on the body. (b) First row of the complex modal coordinate ensemble matrix \mathbf{q} encompassing the undulation frequency information. One revolution indicates one complete period of undulation of the mode. (c) The complex numbers indicated in (a) are visualized as unwrapped angles to quantify the average whirl rate. The slope of the best-fit line is the number of spatial periods ν . The slope for the vertical wave ψ is twice as great as for the horizontal wave θ . (d) The slope of the line indicates the number of undulation periods during the glide. The slope of the vertical bending wave line is twice as great as the horizontal bending wave line.

Orientation of the body

We specify the orientation of the co-moving frame using Euler angles and the time evolution of these angles with the kinematic differential equations. Traditional aircraft Euler angles (3-2-1 Euler angles) use three successive rotations about the yaw, pitch, and roll axes, with the yaw axis (z -axis) pointing downward, the pitch axis (y -axis) to the right, and the roll axis (x -axis) through the front of the aircraft. Because we have modified the co-moving frame such that the z -axis is vertical, the y -axis is the forward direction, and the x -axis is to the right, we use the same notation, but modify the rotation order to keep the same convention of positive pitch, resulting in a nose-up rotation and a positive roll resulting in rotation to the right. We therefore use 2-1-3 Euler angles as defined in [7] to construct a rotation matrix that rotates vectors in the inertial frame into the body frame,

$$\hat{\mathbf{b}} = \mathbf{C}\hat{\mathbf{n}} \quad \hat{\mathbf{n}} = \mathbf{C}^T\hat{\mathbf{b}} \quad (\text{S17})$$

where $\hat{\mathbf{b}}$ signifies quantities in the co-moving (body) frame, $\hat{\mathbf{n}}$ signifies quantities in the inertial frame, and $(\cdot)^T$ is the matrix transpose. The rotation matrix is found by successive pre-multiplications of rotations about each axis,

$$\mathbf{C} = \mathbf{C}_2(\phi)\mathbf{C}_1(\theta)\mathbf{C}_3(\psi) \quad (\text{S18})$$

where a rotation about the pitch axis (x -axis) is

$$\mathbf{C}_1(\theta) = \begin{bmatrix} 1 & 0 & 0 \\ 0 & \cos \theta & \sin \theta \\ 0 & -\sin \theta & \cos \theta \end{bmatrix} \quad (\text{S19})$$

a rotation about the roll axis (y -axis) is

$$\mathbf{C}_2(\phi) = \begin{bmatrix} \cos \phi & 0 & -\sin \phi \\ 0 & 1 & 0 \\ \sin \phi & 0 & \cos \phi \end{bmatrix} \quad (\text{S20})$$

and a rotation about the yaw axis (z -axis) is

$$\mathbf{C}_3(\psi) = \begin{bmatrix} \cos \psi & \sin \psi & 0 \\ -\sin \psi & \cos \psi & 0 \\ 0 & 0 & 1 \end{bmatrix} \quad (\text{S21})$$

Singularities occur with any Euler angle convention. For our convention, we limit angles to

$$0 \leq \psi < 2\pi, \quad \frac{\pi}{2} \leq \theta \leq \frac{\pi}{2}, \quad 0 \leq \phi < 2\pi$$

Therefore, the snake pointing vertically upwards or downwards results in a singularity. However, this condition is never reached in the simulations, as we stop the simulation when any of the angles exceed 85° .

For completeness, the Euler angle accelerations are found by taking the inertial derivative of the kinematic differential equations and applying the product rule,

$$\ddot{\theta} = \dot{\mathbf{K}}\mathbf{C}\vec{\omega} + \mathbf{K}\dot{\mathbf{C}}\vec{\omega} + \mathbf{K}\mathbf{C}\dot{\vec{\omega}} \quad (\text{S22})$$

The derivative of the rotation matrix is derived from the complete set of Poisson equations [8]

$$\dot{\mathbf{C}} = -{}^B\tilde{\omega}\mathbf{C} \quad (\text{S23})$$

where ${}^B\tilde{\omega}$ is the cross product matrix of the angular velocity expressed in the co-moving frame coordinate system given as

$${}^B\tilde{\omega} = \begin{bmatrix} 0 & -\omega_z & \omega_y \\ \omega_z & 0 & -\omega_x \\ -\omega_y & \omega_x & 0 \end{bmatrix} \quad (\text{S24})$$

The angular acceleration $\dot{\vec{\omega}}$ is an output of the dynamics simulation and is therefore readily available. The derivative of the kinematic differential equations is

$$\dot{\mathbf{K}} = \frac{1}{c_\theta} \begin{bmatrix} -\dot{\theta}s_\phi t_\theta - \dot{\phi}c_\phi & 0 & \dot{\theta}c_\phi t_\theta - \dot{\phi}s_\phi \\ -\dot{\phi}s_\phi c_\theta & 0 & \dot{\phi}c_\phi c_\theta \\ \dot{\phi}c_\phi s_\theta + \dot{\theta}s_\phi/c_\theta & \dot{\phi}/c_\theta & \dot{\phi}s_\phi s_\theta - \dot{\theta}c_\phi/c_\theta \end{bmatrix} \quad (\text{S25})$$

where $s_{(\cdot)}$, $c_{(\cdot)}$, and $t_{(\cdot)}$ are the sine, cosine, and tangent of the respective angle. Combining the above expressions, the final form of the Euler angle accelerations is

$$\ddot{\theta} = \dot{\mathbf{K}}\mathbf{C}\vec{\omega} - \mathbf{K}{}^B\tilde{\omega}\mathbf{C}\vec{\omega} + \mathbf{K}\mathbf{C}\dot{\vec{\omega}} \quad (\text{S26})$$

To specify simulation initial conditions (discussed below), we rearrange the kinematic differential equations,

$$\dot{\theta} = \mathbf{K}^B\vec{\omega} = \mathbf{K}\mathbf{C}\vec{\omega} \quad (\text{S27})$$

to solve for the angular velocity. The resulting expression is

$${}^B\vec{\omega} = \mathbf{K}^{-1}\dot{\vec{\theta}} \quad (\text{S28})$$

where the inverse of the kinematic differential equations is

$$\mathbf{K}^{-1} = \begin{bmatrix} -\cos\theta \sin\phi & \cos\phi & 0 \\ \sin\theta & 0 & 1 \\ \cos\theta \cos\phi & \sin\phi & 0 \end{bmatrix} \quad (\text{S29})$$

Lastly, the yaw, pitch, and roll angles can be extracted from the components of the rotation matrix \mathbf{C} as

$$\begin{bmatrix} \psi \\ \theta \\ \phi \end{bmatrix} = \begin{bmatrix} \text{atan2}(-c_{21}, c_{22}) \\ \text{asin}(c_{23}) \\ \text{atan2}(-c_{13}, c_{33}) \end{bmatrix} \quad (\text{S30})$$

where c_{ij} are components of \mathbf{C} .

Extending the lift and drag coefficients

The experimentally available lift and drag coefficients were measured over an angle-of-attack range of -10° to 60° [1], while the simulation needs values up to 90° . We extrapolated the measured lift and drag coefficients over this 30° range by first modeling the drag coefficient in the extrapolated region as a parabola with the vertex at 90° .

$$C_D(\alpha) = a_D\alpha^2 + b_D\alpha + c \quad (\text{S31})$$

with the constraints

$$C_D(\alpha = 90^\circ) = C_{D,90^\circ} \text{ from theory/experiments} \quad (\text{S32})$$

$$C_D(\alpha = 60^\circ) = C_{D,60^\circ} \text{ from experiments} \quad (\text{S33})$$

The first (vertex) constraint can be written as

$$\frac{-b_D}{2a_D} = 90 \quad (\text{S34})$$

$$c_D - \frac{b_D^2}{4a_D} = C_{D,90^\circ} \quad (\text{S35})$$

which implies

$$b_D = -180a_D \quad c_D = C_{D,90^\circ} + \frac{b_D^2}{4a_D} \quad (\text{S36})$$

The second constraint implies

$$a_D \cdot 60^2 + b_D \cdot 60 + c_D = C_{D,60^\circ}, \quad (\text{S37})$$

which rearranging for a_D yields

$$a_D = \frac{C_{D,60^\circ} - C_{D,90^\circ}}{60^2 - 180 \cdot 60 + 180^2/4} \quad (\text{S38})$$

To close the equations, $C_{D,90^\circ}$ is estimated to be between 2–2.1 for triangular shapes in the highest-drag configuration [9, Chaper 3, figure 33], with the particular value specified by the Reynolds number (evenly selected between 2 and 2.1 for the seven Reynolds numbers measured in experiments).

The lift coefficient is approximated with a third-order polynomial

$$C_L(\alpha) = a_L\alpha^3 + b_L\alpha^2 + c_L\alpha + d_L \quad (\text{S39})$$

with the constraints

$$C_L(\alpha = 90^\circ) = 0 \quad (\text{S40})$$

$$C_L(\alpha = 60^\circ) = C_{D,60^\circ} \text{ from experiments} \quad (\text{S41})$$

$$\frac{\partial C_L}{\partial \alpha}(\alpha = 60^\circ) = \frac{\partial C_{L,60^\circ}}{\partial \alpha} \text{ from experiments} \quad (\text{S42})$$

where the lift coefficient derivative is determined by second-order accurate finite differences,

$$\frac{\partial C_{L,60^\circ}}{\partial \alpha} = \frac{3}{2}C_{L,60^\circ} - 2C_{L,55^\circ} + \frac{1}{2}C_{L,50^\circ} \quad (\text{S43})$$

We have an underdetermined system, as we need to determine four parameters for the polynomial, but have only three constraint equations. We solve this in matrix form using a least-squares solution to the system

$$\begin{bmatrix} 0 \\ C_{D,60^\circ} \\ \frac{\partial C_{L,60^\circ}}{\partial \alpha} \end{bmatrix} = \begin{bmatrix} 90^3 & 90^2 & 90 & 1 \\ 60^3 & 60^2 & 60 & 1 \\ 3 \cdot 60^2 & 2 \cdot 60 & 0 & 0 \end{bmatrix} \begin{bmatrix} a_L \\ b_L \\ c_L \\ d_L \end{bmatrix} \quad (\text{S44})$$

To calculate the lift and drag values, we use bivariate splines with no smoothing (linear interpolation) to form two two-dimensional surfaces that are evaluated at (α, Re) separately for each location along the body. If $Re < Re_{\min}$ or $Re > Re_{\max}$, the Reynolds number is set to within these bounds.

References

- [1] Holden, D., Socha, J. J., Cardwell, N. D. & Vlachos, P. P. Aerodynamics of the flying snake *Chrysopelea paradisi*: how a bluff body cross-sectional shape contributes to gliding performance. *J Exp Biol* **217**, 382–394 (2014).
- [2] Socha, J. J. Gliding flight in the paradise tree snake. *Nature* **418**, 603–604 (2002).
- [3] Socha, J. J. & LaBarbera, M. Effects of size and behavior on aerial performance of two species of flying snakes (*Chrysopelea*). *J Exp Biol* **208**, 1835–1847 (2005).
- [4] Feeny, B. F. A complex orthogonal decomposition for wave motion analysis. *J Sound Vib* **310**, 77–90 (2008).
- [5] Feeny, B. F. & Feeny, A. K. Complex modal analysis of the swimming motion of a whiting. *J Vib Acoust.* **135** (2013).
- [6] Feeny, B. F., Sternberg, P. W., Cronin, C. J. & Coppola, C. A. Complex orthogonal decomposition applied to nematode posturing. *J Comput Nonlinear Dyn* **8** (2013).
- [7] Diebel, J. Representing attitude: Euler angles, unit quaternions, and rotation vectors. *Matrix* **58**, 1–35 (2006).
- [8] Greenwood, D. T. *Advanced Dynamics* (Cambridge University Press, 2006).
- [9] Hoerner, S. F. *Fluid-dynamic Drag: Practical Information on Aerodynamic Drag and Hydrodynamic Resistance* (Hoerner Fluid Dynamic, 1965).